Low-energy electrons (5–50 keV) in the inner magnetosphere

N. Y. Ganushkina,[1,2] M. W. Liemohn,[2] O. A. Amariutei,[1] and D. Pitchford[3]

Received 9 August 2013; revised 25 November 2013; accepted 28 November 2013; published 22 January 2014.

[1] Transport and acceleration of the 5–50 keV electrons from the plasma sheet to geostationary orbit were investigated. These electrons constitute the low-energy part of the seed population for the high-energy MeV particles in the radiation belts and are responsible for surface charging. We modeled one nonstorm event on 24–30 November 2011, when the presence of isolated substorms was seen in the *AE* index. We used the Inner Magnetosphere Particle Transport and Acceleration Model (IMPTAM) with the boundary at 10 R_E with moment values for the electrons in the plasma sheet. The output of the IMPTAM modeling was compared to the observed electron fluxes in 10 energy channels (from 5 to 50 keV) measured on board the AMC 12 geostationary spacecraft by the Compact Environmental Anomaly Sensor II with electrostatic analyzer instrument. The behavior of the fluxes depends on the electron energy. The IMPTAM model, driven by the observed parameters such as Interplanetary Magnetic Field (IMF) B_y and B_z, solar wind velocity, number density, dynamic pressure, and the *Dst* index, was not able to reproduce the observed peaks in the electron fluxes when no significant variations are present in those parameters. We launched several substorm-associated electromagnetic pulses at the substorm onsets during the modeled period. The observed increases in the fluxes can be captured by IMPTAM when substorm-associated electromagnetic fields are taken into account. Modifications of the pulse front velocity and arrival time are needed to exactly match the observed enhancements.

Citation: Ganushkina, N. Y., M. W. Liemohn, O. A. Amariutei, and D. Pitchford (2014), Low-energy electrons (5–50 keV) in the inner magnetosphere, *J. Geophys. Res. Space Physics*, *119*, 246–259, doi:10.1002/2013JA019304.

1. Introduction

[2] The fluxes of electrons with energies from about 5 to 50 keV are not usually analyzed in details when studying the electron radiation belts. These fluxes constitute the low-energy part of the seed population, which is critically important for radiation belt dynamics. It is through cyclotron resonance with the electrons of energies between a few and tens of keV [*Kennel and Petschek*, 1966; *Kennel and Thorne*, 1967; *Li et al.*, 2008, 2012] that chorus waves are generated outside the plasmapause in association with the injection of plasma sheet electrons into the inner magnetosphere [*Tsurutani and Smith*, 1974; *Meredith et al.*, 2001]. Whistler mode chorus waves play an important role in accelerating the seed electron population to relativistic energies in the outer radiation belt [*Horne et al.*, 2005; *Chen et al.*, 2007]. Radiation belt models need to specify the flux at a low-energy boundary at all L shells. Moreover, energetic electrons with energies less than about 100 keV are responsible for hazardous space-weather phenomena such as surface charging [*Purvis et al.*, 1984; *Whipple*, 1981; *Garrett*, 1981; *Davis et al.*, 2008]. This has been the cause of anomalies, for example, on satellites in geosynchronous orbit [*Frezet et al.*, 1988; *Hoeber et al.*, 1998; *Koons et al.*, 1999]. The electron flux at these 5 to 50 keV energies varies significantly with geomagnetic activity and even during quiet time periods.

[3] The geostationary electron model IGE-2006 was developed by *Sicard-Piet et al.* [2008] for the wide range of energies from 1 keV to 5.2 MeV. Data from all the instruments from the geosynchronous orbit satellites operated by the Los Alamos National Laboratory (LANL) over the period from 1976 to 2006 in combination with the data from the Japanese geostationary spacecraft, Data Relay Test Satellite, were used. This new model allows one to obtain electron fluxes over a solar cycle, and it can be used for any mission longer than 1 year. Comparison to the NASA AE 8 model revealed that the model electron fluxes are higher than those given by the AE 8 model for the low-energy channels (<100 keV). At the same time, the usage of this climatological model for specific cases is problematic.

[4] The source of the low-energy electrons is the plasma sheet. *Korth et al.* [1999] have analyzed the data from the Magnetospheric Plasma Analyzer (MPA) instruments [*Bame et al.*, 1993] on three LANL satellites for a statistical

[1]Finnish Meteorological Institute, Helsinki, Finland.
[2]Department of Atmospheric, Oceanic and Space Sciences, University of Michigan, Ann Arbor, Michigan, USA.
[3]Power/Thermal Subsystems and Spacecraft Survivability SES ENGINEERING, L-6815 Château de Betzdorf, Luxembourg.

Corresponding author: N. Y. Ganushkina, Finnish Meteorological Institute, Helsinki, FI-00101, Finland. (Natalia.Ganushkina@fmi.fi)

2169-9380/14/10.1002/2013JA019304

study of electron fluxes with energies between 1 eV and 45 keV at geosynchronous orbit and their dependence on local time and geomagnetic activity level as measured by *Kp*. They calculated the positions of the separatrix between open and closed drift trajectories as a function of particle energy, local time, and geomagnetic activity level. The comparisons confirmed the predictions of plasma sheet access to the geosynchronous region. *Friedel et al.* [2001] analyzed the electron data from the Polar Hydra instrument [*Scudder et al.*, 1995] using its coverage of the inner magnetospheric region at radial distances from 2 to 9 R_E and geosynchronous data measured by the LANL MPA sensors. They showed that the simple corotation and convection electric field can describe rather well the average properties of transport for these particles for a wide range of geomagnetic activity and over a large part of the inner magnetosphere. As it was shown by *Thomsen et al.* [2002], the sharp upper edge of the nightside electron plasma sheet energy distribution observed at geosynchronous orbit by LANL MPA can provide a measure of the effective strength of the convection electric field that transports plasma sheet material into the inner magnetosphere. They found that the temporal profile of convection typically consists of a sequence of bursts, where each convection enhancement lasts no more than a fraction of an hour. According to simultaneous multipoint measurements, these convection enhancements are observed first near midnight and then propagate sunward with speeds of 5–30 km/s. *Denton et al.* [2005] presented a comprehensive study of plasma properties at geosynchronous orbit between 1990 and 2001 using LANL MPA data. They found that the electron densities are greatest in the dawn region for the periods of highest convection. They demonstrated that the density of electrons in the plasma sheet is strongly dependent upon the magnetospheric convection strength and upon solar activity. Electron density at geosynchronous orbit is strongly correlated with solar activity. Observational studies using the electron data from the Time History of Events and Macroscale Interactions during Substorms (THEMIS) spacecraft [*Kurita et al.*, 2011] and particle-tracing studies [*Elkington et al.*, 2004; *Miyoshi et al.*, 2006] reconfirmed the previous results on the large-scale convection electric field controlling the electron transport to the inner magnetosphere. Furthermore, several studies have noted the existence of localized and short-lived flow channels in the electric potential patterns from the assimilative mapping of ionospheric electrodynamics (AMIE) model [e.g., *Boonsiriseth et al.*, 2001; *Chen et al.*, 2003; *Khazanov et al.*, 2004a, 2004b].

[5] Significant variations in the low-energy electrons can be seen during isolated substorms, not related to any storm periods. Moreover, electron flux variations depend on the electron energy. Early studies using observations from Russian Raduga communication geostationary satellites [*Vakulin et al.*, 1988; *Grafodatskiy et al.*, 1987] and modeling efforts [*Degtyarev et al.*, 1990] have shown that under magnetically quiet conditions the features of the spatial distribution of low-energy electrons along the geostationary orbit are due to isolated substorm disturbances.

[6] *Kozelova et al.* [2006] used data from the Combined Release and Radiation Effects Satellite (CRRES) to examine the dynamics of low energy (100 eV to 30 keV) ions and electrons using Low Energy Plasma Analyzer (LEPA) data [*Hardy et al.*, 1993] near the onset of the substorm on 12 March 1991. CRRES was located on L = 6.3 (and at 21.5 magnetic local time (MLT)) near the earthward edge of the plasma sheet. It was shown that the electron fluxes with energies from 0.213 keV to 1.88 keV increase during the substorm growth phase. The electron flux is almost constant in the energy range from 2.47 keV to 5.57 keV. The electron flux decreases in the energy range from 7.31 keV to 16.5 keV. At substorm onset, the electron flux in four adjacent energy channels in the range of 7.31–16.5 keV grows sharply and exceeds the level which it had before the beginning of the growth phase. The second injection of 21.7–28.5 keV electrons occurs during the substorm expansion phase.

[7] Observations show that substorm-associated electric fields are usually very complex [*Maynard et al.*, 1996] and can be intense with a strong impulsive component with amplitudes of up to even several tens of mV/m [*Aggson et al.*, 1983; *Cattell and Mozer*, 1984; *Wygant et al.*, 1998; *Rowland and Wygant*, 1998; *Tu et al.*, 2000]. Injections of energetic particles and dipolarization of the magnetic field are well-known signatures of a substorm in the near-Earth space. Several models have been proposed to explain particle injections [*Li et al.*, 1998; *Zaharia et al.*, 2000; *Sarris et al.*, 2002]. So far, these models give good agreement with the observed dispersionless electron injections at geostationary orbit [*Ingraham et al.*, 2001; *Li et al.*, 2003; *Mithaiwala and Horton*, 2005; *Liu et al.*, 2009]. Recently, *Ganushkina et al.* [2013] investigated the transport and acceleration of low-energy electrons (50–250 keV) from the plasma sheet to geostationary orbit. It was found that the large-scale convection in combination with substorm-associated impulsive fields are the drivers of the transport of plasma sheet electrons from 10 R_E to geostationary orbit at 6.6 R_E during storm times. Similarly, *Fok et al.* [2001] conducted numerical studies of rapid enhancements of radiation belt electron fluxes due to substorm dipolarizations, and *Khazanov et al.* [2004b] found that electric field fluctuations could provide substantial increases in inner magnetospheric electron seed population fluxes.

[8] Up to now, there have been only a few studies on the details of the responses of certain energy channels when measuring electrons below 50 keV to substorm variations during nonstorm periods. In the present paper, we investigate the low-energy electron (5–50 keV) transport and acceleration from the plasma sheet to geostationary orbit. We specifically study the roles of large-scale convection and substorm-associated fields. We use the Inner Magnetosphere Particle Transport and Acceleration model (IMPTAM) [*Ganushkina et al.*, 2001, 2005, 2006, 2012] with the boundary at 10 R_E in the plasma sheet, where we set boundary conditions for the low-energy electrons following *Tsyganenko and Mukai* [2003]. We model one rather quiet event on 24–30 November 2011, when isolated substorms were present in the *AE* index. The significant variations seen in the observed fluxes can be associated only with substorm activity. We follow the evolution of the electron distribution function from 10 R_E to 6.6 R_E, and we launch a series of substorm-associated electromagnetic pulses at substorm onsets to represent the changes, which occur during substorm dipolarizations. The output of the IMPTAM modeling is compared to the observed electron fluxes in 10 energy

channels (5–50 keV) measured at geostationary orbit. We present and discuss the different responses of these energy channels to the substorm activity during this nonstorm event.

2. Event Overview

[9] The event on 24–30 November 2011 (Figure 1) was, in general, rather quiet but with the signatures of substorm activity. During the first 3 days, the Interplanetary Magnetic Field (IMF) B_z (Figure 1a) oscillated around zero, not exceeding ±5 nT. The solar wind velocity (Figure 1b) was also quite stable, about 400 km/s. The solar wind dynamic pressure (Figure 1c) was about 1.2 nPa with few variations. The *Kp* index (Figure 1d) reached 3 at the end of 24 November, and it was not more than 2 during the next 2 days. There were two substorm activations seen in the *AE* index (Figure 1e) with peaks of about 500 nT around 1800 UT and 2200 UT on 24 November, when the IMF B_z showed turns to negative values. On 25 and 26 November, several peaks in the *AE* index with less than 200 nT values are seen. The *SYM-H* index (Figure 1f) was around –20 nT from the end of 24 November through the beginning of 25 November and, then, close to zero. During 27 November, two periods of short negative IMF B_z of about –5 nT corresponded to two substorm activations with *AE* peaks of 700 nT at around 0800 UT and 800 nT at around 1700 UT. Solar wind speed increased from 350 km/s to 470 km/s during that day. Solar wind dynamic pressure reached 4 nPa at around 1000 UT, *Kp* was 2, and *SYM-H* was about –15 to –20 nT.

[10] The largest variations were observed at the end of 28 November to the beginning of 29 November. IMF B_z dropped to –11 nT at around 2300 UT on 28 November and then jumped to +13 nT at around 0300 UT on 29 November. At the same time with the IMF B_z drop, the solar wind velocity increased sharply from 350 km/s to 530 km/s. Simultaneously, solar wind dynamic pressure reached 6 nPa at 2330 UT. *Kp* became equal to 4, *AE* displayed a peak of 500 nT, and *SYM-H* dropped from +20 nT to –20 nT. During the last 2 days of the event, there were several negative turns in IMF B_z reaching about –7 nT. Solar wind speed was at the level of about 430 km/s. Solar wind dynamic pressure displayed two peaks of about 12 nPa at 0200 and 0600 UT on 29 November then was about 4 nPa and decreased to 1.3 nPa on 30 November. *Kp* was around 3 and *Dst* showed variations of –30 nT reaching –40 nT at the end of 30 November. Substorm activations were seen in *AE* with peaks of 650 nT at about 0700 UT and 750 nT at about 1700 UT on 29 November. More prolonged activation started at about 1100 UT on 30 November with 800 nT and reached 940 nT at 1800 UT. The last peak was of 400 nT at about 2300 UT.

3. Instrumentation and Data

[11] The data which we analyze in the present paper come from the AMC 12 geostationary satellite which was at 322.5°E. The AMC 12 satellite has a CEASE II (Compact Environmental Anomaly Sensor) instrument [*Dichter et al.*, 1998], which contains an electrostatic analyzer (ESA) and is a suite of various sensors intended to measure the in situ space environment at the host spacecraft. The instrument contains a Lightly Shielded Dosimeter, a Heavily Shielded Dosimeter, a Particle Telescope (measuring high-energy electrons and protons), and an electrostatic analyzer for measuring low-energy electron fluxes in 10 channels, covering the range 5–50 keV.

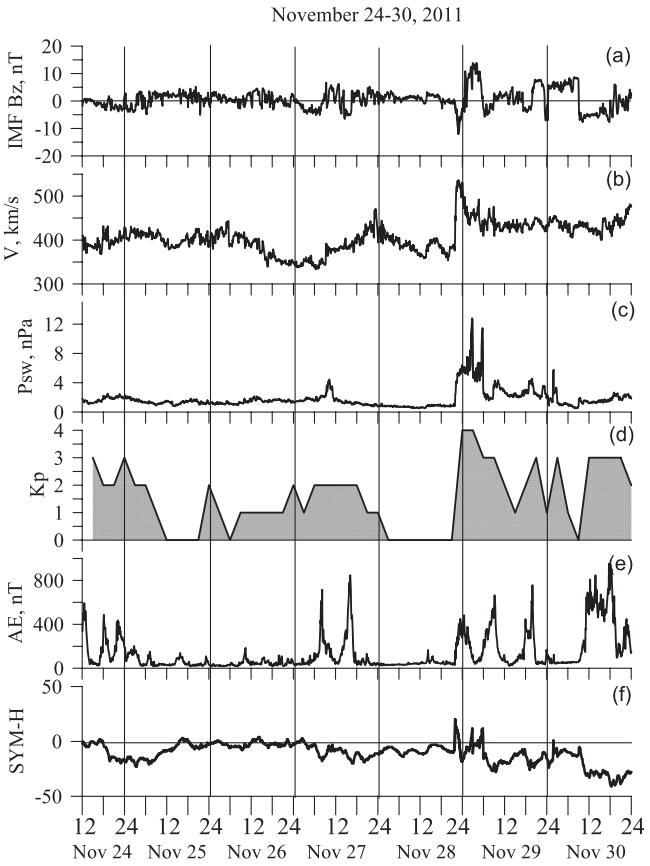

Figure 1. Overview of the modeled event on 24–30 November 2011.

[12] The CPA (Charge Plate Assembly) sensor [*Bogorad et al.*, 1995] is used to measure the surface charging effect that is due to these keV-energy electrons. This sensor was at another geostationary spacecraft, NSS-803, which was at 340°E (roughly 1 h of local time to the east), and the signatures from the CEASE II and CPA sensors can be compared under the assumption that both satellites are exposed to the same charged particle environment. During the periods of increased low-energy electron fluxes, there exist the clear increase in the spacecraft potential magnitudes.

4. Modeling Approach

4.1. Inner Magnetosphere Particle Transport and Acceleration Model

[13] The Inner Magnetosphere Particle Transport and Acceleration model (IMPTAM), developed by *Ganushkina et al.* [2001, 2005, 2006], simulates distributions of ions and electrons with arbitrary pitch angles moving from the plasma sheet to the inner *L* shell regions. Particles with energies up to hundreds of keVs are followed in time-dependent magnetic and electric fields. Recently, a detailed description was presented in *Ganushkina et al.* [2012, 2013].

[14] We consider the drift velocity as a combination of the $\mathbf{E} \times \mathbf{B}$ drift velocity and the velocities of gradient and

curvature drifts. We assume that the first and second adiabatic invariants are conserved. We consider the bounce-average drift velocity after averaging over one bounce of $\mathbf{E} \times \mathbf{B}$ magnetic drift velocities [*Roederer*, 1970]

$$\langle v_0 \rangle = \frac{\mathbf{E_0} \times \mathbf{B_0}}{B_0^2} + \frac{2p}{q\tau_b B_0} \nabla I \times \mathbf{e_0}, \quad (1)$$

where $\mathbf{E_0}$ and $\mathbf{B_0}$ are the electric and magnetic fields in the equatorial plane, respectively, p is the particle's momentum, τ_b is the particle's bounce period, $I = \int_{S_m}^{S'_m} \left[1 - \frac{B(s)}{B_m}\right]^{1/2} \mathrm{d}s$, S_m, and S'_m are the mirror points, $B(s)$ is the magnetic field along the magnetic field line, B_m is the magnetic field at the mirror point, $\mathbf{e_0}$ is the unit vector in the direction of the magnetic field $\mathbf{B_0}$.

[15] The changes in the distribution function $f(R, \phi, t, E_{\mathrm{kin}}, \alpha)$, where R and ϕ are the radial and azimuthal coordinates in the equatorial plane, respectively, t is the time, E_{kin} is the particle energy, and α is the particle pitch angle, are obtained by solving the following equation:

$$\frac{\mathrm{d}f}{\mathrm{d}t} = \frac{\partial f}{\partial \phi} \cdot V_\phi + \frac{\partial f}{\partial R} \cdot V_R + \text{sources} - \text{losses}, \quad (2)$$

where V_ϕ and V_R are the azimuthal and radial components of the bounce-average drift velocity. Liouville's theorem is used to gain information of the entire distribution function with losses taken into account.

[16] For the obtained distribution function, we apply radial diffusion [*Fälthammar*, 1965; *Schulz and Lanzerotti*, 1974; *Brautigam and Albert*, 2000] by solving the radial diffusion equation [*Schulz and Lanzerotti*, 1974] for the distribution function from equation (2):

$$\frac{\partial f}{\partial t} = L^2 \frac{\partial}{\partial L}\left(L^{-2} D_{LL} \frac{\partial f}{\partial L}\right) - \frac{f}{\tau_{\mathrm{eL}}}, \quad (3)$$

where τ_{eL} is the electron lifetime, and D_{LL} is the radial diffusion coefficient. *Kp*-dependent radial diffusion coefficients D_{LL} for the magnetic field fluctuations are computed following *Brautigam and Albert* [2000] using

$$D_{LL} = 10^{0.056Kp - 9.325} L^{10}. \quad (4)$$

Since diffusion by the magnetic field fluctuations at $L > 3$ dominates diffusion produced by electrostatic field fluctuations [*Shprits and Thorne*, 2004], we ignore the electrostatic component of the radial diffusion coefficient [*Lejosne et al.*, 2013].

[17] At the next time step we repeat the order of calculation: First, we solve transport with losses with equation (2) and then apply diffusion with equation (3).

[18] The goal of this study is to investigate how the substorm-associated fields can be responsible for the access of plasma sheet electrons with low energies (<50 keV) to the geostationary orbit during quiet times. For electron losses we consider convection outflow, when a particle intersects the magnetopause and moves away from the modeled region, and pitch angle diffusion, when particles are lost to the atmosphere due to pitch angle scattering. To represent the pitch angle diffusion, we introduce the electron lifetimes. We use the *Chen et al.* [2005] electron lifetimes for strong diffusion as

$$\tau_{sd} = \left(\frac{\gamma m_0}{p}\right)\left[\frac{2\Psi B_h}{1-\eta}\right], \quad (5)$$

where p is the particle momentum, γ is the ratio of relativistic mass to rest mass, B_h is the magnetic field at either foot point of the field line, Ψ is the magnetic flux tube volume, $\eta = 0.25$ is the backscatter coefficient (25% of electrons that will mirror at or below 0.02 R_E are scattered back to the flux tube instead of precipitating into the atmosphere). We use the *Shprits et al.* [2007] electron lifetimes for weak diffusion as

$$\tau_{wd} = 4.8 \cdot 10^4 B_w^2 L^{-1} E^2, \; B_w^2 = 2 \cdot 10^{2.5 + 0.18Kp}, \quad (6)$$

where B_w is the local wave amplitude and E is kinetic energy in MeV.

[19] Sources for the modeling are particles in the plasma sheet which are constantly coming to the inner magnetosphere regions. We set the model boundary at 10 R_E and use the kappa electron distribution function (k = 1.5) with number density n and temperature T given by the empirical model derived from Geotail data by *Tsyganenko and Mukai* [2003]. The results presented as a part of the review paper by *Horne et al.* [2013] indicated that decreasing k parameter from 5 to 1.5 gave the best agreement between the modeled and the observed electron fluxes with 50–150 keV energies at geostationary orbit. The electron n is assumed to be the same as that for ions in the model but Te/Ti = 0.2 is taken into account (as was shown, for example, in *Kaufmann et al.* [2005] and *Wang et al.* [2012], based on Geotail and THEMIS data). We also introduced a time shift of 2 h following *Borovsky et al.* [1998] for the solar wind material to reach the midtail plasma sheet. The evolution of the modeled electron distributions was followed using a dipole model for the internal magnetic field and T96 [*Tsyganenko*, 1995] model for the external magnetic field with *Dst*, P_{sw}, IMF B_y, and B_z as input parameters. For the large-scale electric field we use the *Boyle et al.* [1997] polar cap potential, dependent on solar wind and IMF parameters, applied to a Volland-Stern [*Volland*, 1973; *Stern*, 1975] type convection electric field pattern. This combination of models was successfully used [*Ganushkina et al.*, 2013] to study the transport and acceleration of 50–250 keV electrons with the comparison to the observed electron fluxes in four energy ranges (50–225 keV) measured on board the LANL spacecraft by the Synchronous Orbit Particle Analyzer (SOPA) instrument.

5. Modeling Results

[20] The output of the IMPTAM modeling was compared to the observed electron fluxes in 10 energy ranges measured onboard AMC 12 spacecraft by the CEASE II ESA instrument for the 24–30 November 2011 event. It should be stressed that the absolute flux values presented here may not be correct due to uncertainties in the sensor geometric factors. When we analyze the data, it is the relative variations of the flux data that we compare, rather than the absolute fluxes. Nevertheless, we compare the values of the observed and modeled fluxes in the paper keeping in mind the above remark. Here we will focus on the data and model output for selected time periods on 25 November and 28–29 November.

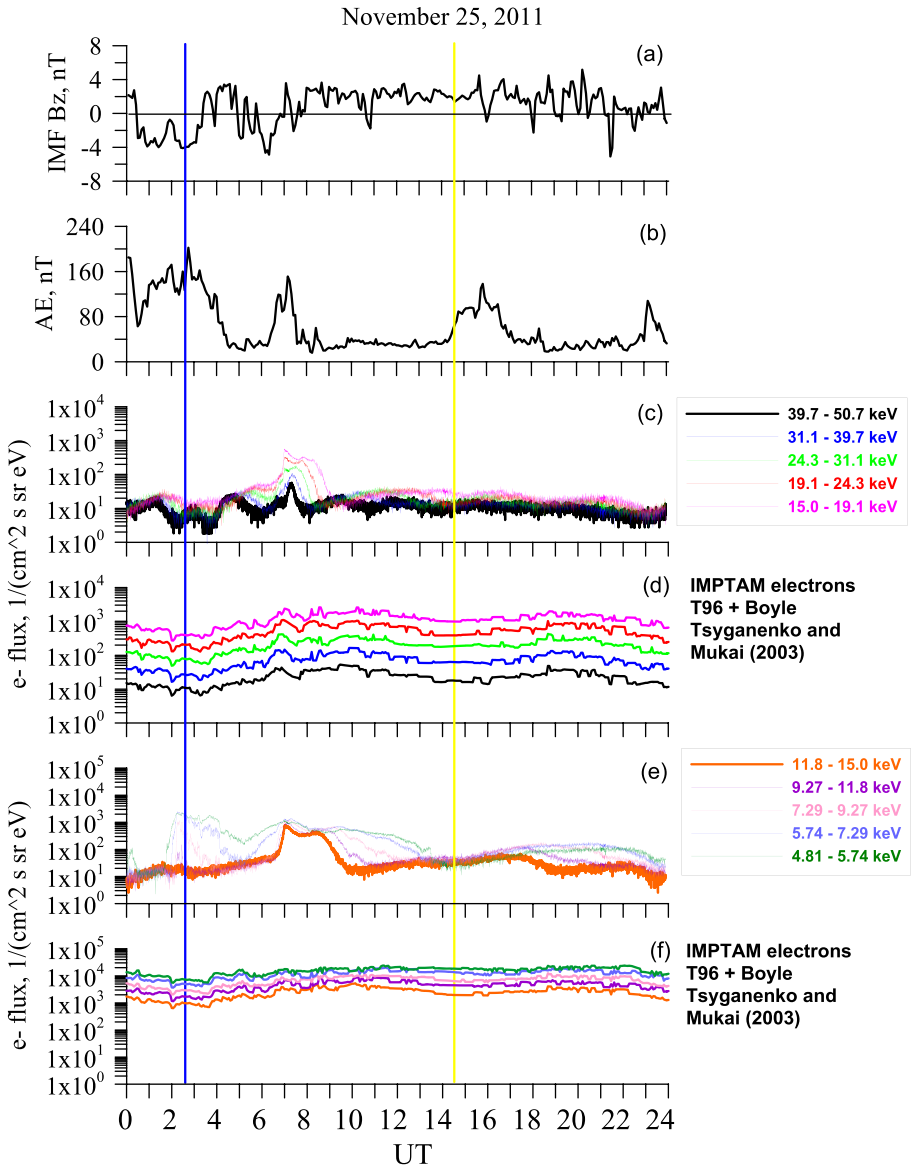

Figure 2. Indications of substorm activity presented as (a) IMF B_z and (b) *AE* index and the observed by the AMC 12 CEASE II ESA instrument and modeled electron fluxes at geostationary orbit during 25 November 2011 event in 10 energy channels: (c and d) 39.7–50.7 keV (black lines), 31.1–39.7 keV (blue lines), 24.3–31.1 keV (green lines), 19.1–24.3 keV (red lines), and 15.0–19.1 keV (pink lines), (e and f) 11.8–15 keV (orange lines), 9.27–11.8 keV (magenta lines), 7.29–9.27 keV (light pink lines), 5.74–7.29 keV (light blue lines), and 4.81–5.74 keV (dark green lines). Blue and yellow vertical lines indicate local midnight and noon, respectively.

[21] The data are in the format of time-averaged differential fluxes (#/(cm^2 sec *sr eV*)). The output from the model is integral flux (#/(cm^2 sec)) produced by all electrons coming from all directions with energies in the 10 given energy ranges. In order to be able to compare the observed and modeled fluxes more properly, we need to introduce the width of the energy channel and the solid angle 4π. So the model electron fluxes are in *model flux*/($4\pi\Delta E$).

5.1. Little or No Variations in Solar Wind and IMF Parameters Driving the Model

[22] First, we concentrate on 25 November 2011 time period out of the 24–30 November 2011 event. Figure 2 presents the data and modeling results for 25 November 2011. Figures 2a and 2b show the observed IMF B_z and *AE* index, respectively. As it can be noticed, variations in IMF B_z were rather small, not more than ±4 nT. Several southward turnings resulted in small substorm activations seen in the *AE* index.

[23] Figure 2c shows the measured electron fluxes at geostationary orbit by the CEASE II ESA instrument on board the AMC 12 satellite in the first five energy channels: 39.7–50.7 keV (black lines), 31.1–39.7 keV (blue lines), 24.3–31.1 keV (green lines), 19.1–24.3 keV (red lines), and 15.0–19.1 keV (pink lines). Figure 2e shows the measured electron fluxes in the other five energy channels:

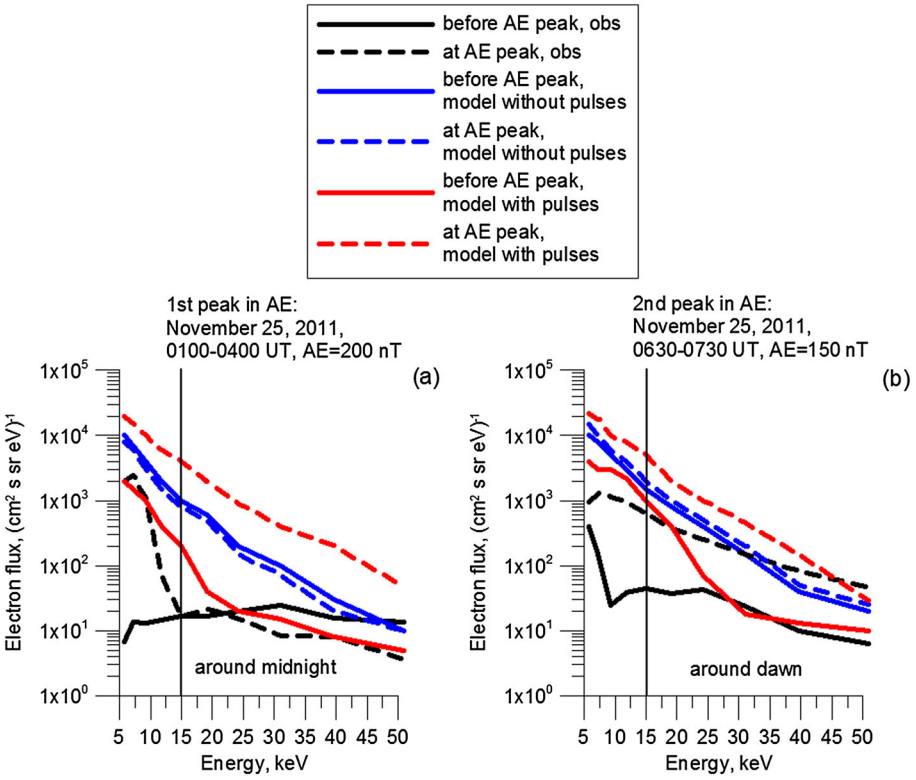

Figure 3. Flux versus energy spectrum of the observed fluxes before the *AE* peak (black lines) and at the peak (dashed black lines), the modeled fluxes without addition of electromagnetic pulses before the peak (blue lines) and at the peak (dashed blue lines), and the modeled fluxes with addition of electromagnetic pulses before the peak (red lines) and at the peak (dashed red lines) for (a) first and (b) second *AE* peaks on 25 November 2011.

11.8–15 keV (orange lines), 9.27–11.8 keV (magenta lines), 7.29–9.27 keV (light pink lines), 5.74–7.29 keV (light blue lines), and 4.81–5.74 keV (dark green lines). Blue and yellow vertical lines indicate local midnight and noon, respectively.

[24] During 25 November there were three disturbance activations seen in *AE* as increases of more than 100 nT: from 0100 to 0400 UT with *AE* about 200 nT, from 0630 to 0730 UT with *AE* about 150 nT, and from 1430 to 1700 UT with *AE* about 140 nT. During the first two activations the satellite was on the nightside moving toward dawn. The observed fluxes are plotted in Figure 3 at 0100 UT (0600 UT) as fluxes before the *AE* peak (black lines) and at 0220 UT (0720 UT) as fluxes at the *AE* peak (dashed black lines) for (a) the first and (b) second peak, respectively. The first activation did not lead to a significant increase of the observed 15–50 keV electron fluxes (Figure 3a, right); it resulted in even lower fluxes at the *AE* peak than before the peak. The second peak in *AE* corresponded to the evident increase of 1 order of magnitude in the observed fluxes in all five energies as compared to the fluxes before the activation (Figure 3b, right). We must keep in mind that during the second *AE* increase, the satellite was not at midnight but well at dawn. During the third activation, the satellite was near noon, so no peaks are seen in the observed fluxes.

[25] Figure 2d presents the modeled electron fluxes obtained using IMPTAM by following the electron distribution from 10 R_E with *Tsyganenko and Mukai* [2003] boundary conditions to the AMC 12 orbit in the combination of the Tsyganenko T96 magnetic field and *Boyle et al.* [1997] electric field models. We start simulations on 24 November 2011 at 1200 UT with an empty magnetosphere. We allow the model to run for 12 h to produce an initial state. For the higher energy range from 15 to 50 keV, the obtained values differ from the observed ones. The closest to the observed values is the electron flux for energies of 39.7–50.7 keV, with the averaged value of 10^1 #/(cm^2 sec *sr eV*). The largest difference is seen for the electron fluxes with energies of 15–19.1 keV: The modeled flux reaches 10^3 #/(cm^2 sec *sr eV*) in average, while the observed peak value is $5.5 \cdot 10^2$ #/(cm^2 sec *sr eV*) (Figure 2c). At the same time, similar to the observations, the flux with the highest energy (39.7–50.7 keV) is the smallest, whereas the flux with lowest energy (15–19.1 keV) has the largest values.

[26] The modeled fluxes are plotted in Figure 3, similar as for the observed fluxes, as fluxes before the *AE* peak (blue lines) and as fluxes at the *AE* peak (dashed blue lines) for (a) the first and (b) second peaks. For 15–50 keV electrons, the modeled electron fluxes do not show any peaks corresponding to the observed ones. For the first *AE* peak (Figure 3a, right), when no increase but rather decrease of fluxes is seen at the *AE* peak, the model fluxes also show a slight decrease. For the second *AE* peak (Figure 3b, right), there is a very small increase in the modeled fluxes at the *AE* peak as compared to the modeled fluxes before the *AE* peak but not a significant increase corresponding to observations.

[27] Next, Figure 2e shows the behavior of the observed electron fluxes in the last five energy ranges, from 5 to 15 keV. The noticeable difference from Figure 2c is the presence of a peak corresponding to the first increase in *AE*. Around 0200 UT, when fluxes of the 15–50 keV electrons have a minimum, fluxes in four energy ranges from 12 to 4 keV increase rather sharply. Compared to the fluxes before the activation, the fluxes reached in their peak the increase of 2 orders of magnitude. In Figure 3a (left), a clear jump of the observed fluxes at the *AE* peak is present, while no difference between the before *AE* peak and at *AE* peak fluxes is seen for 11.8–15 keV electrons. Thus, the first peak corresponding to the first increase in *AE* was observed only in electron fluxes with energies below 12 keV. The satellite was very close to midnight at that time.

[28] In the peak corresponding to the second *AE* increase, the observed fluxes of all five energies reached values of $7 - 11 \cdot 10^2$ #/(cm^2 sec *sr eV*), less than an order of difference as for higher energies in Figure 2c. A sharp increase in the fluxes from about $2 - 4 \cdot 10^1$ #/(cm^2 sec *sr eV*) was seen only for electrons with energies from 15 to 7 keV. Two lower energy channels showed a more gradual increase and also a gradual decrease. The fluxes stayed increased for a longer time, they all became of the same magnitude of $3.5 \cdot 10^2$ #/(cm^2 sec *sr eV*) again only after 7 h, whereas for the peak in Figure 2c, it took 3 h. As can be seen in Figure 3b (left) before the *AE* peak, the fluxes of lower energy electrons (< 7 keV) were of one order of magnitude higher than the fluxes with other energies and their increase at the *AE* peak was different as was mentioned above.

[29] Figure 2f presents the modeled electron fluxes for the energy ranges as in Figure 2e. Similar to Figure 2d, the modeled electron fluxes do not show any peaks corresponding to the observed ones (see also Figure 3b, left). The values of the modeled fluxes are about 1 order of magnitude higher in average than the observed ones. The flux of electrons with energies of 11.8–15 keV is the lowest, whereas the flux of electrons with energies of 4.81–5.74 keV is the highest.

[30] IMPTAM includes three models, namely, for boundary conditions, magnetic and electric fields, which depend on IMF and solar wind parameters and Dst. The variations in the modeled fluxes are determined by the variations of the models' parameters. Since no variations were observed in IMF B_y and B_z, solar wind velocity, number density and dynamic pressure, and *Dst* index, the model fluxes do not change much. The observed peaks cannot be reproduced in IMPTAM by the changes in driving conditions for the modeled electrons; it is not the drifts caused by the large-scale electric and magnetic fields.

5.2. Presence of Variations in Solar Wind and IMF Parameters Driving the Model

[31] Figure 4 presents another example of the low-energy electron fluxes measured onboard AMC 12. We will concentrate on the end of 28 November to the beginning of 29 November. Almost the whole day on 28 November was very quiet with IMF B_z close to zero, with solar wind dynamic pressure of 1 nPa, $Kp = 0$, and no increases in *AE*. Starting from 2200 UT, IMF B_z turned southward and reached –12 nT in 1 h (Figure 4a). At the same time *AE* started to rise and became about 440 nT at about 2315 UT (Figure 4b). IMF B_z became positive at the end of 28 November and reached 13 nT around 0300 UT on 29 November. By that time the *AE* index decreased to its undisturbed level after reaching 480 nT.

[32] The observed electron fluxes with energies from 15 to 50 keV were at the level of 10^1 #/(cm^2 sec *sr eV*) on average. Close to the time when IMF B_z started to become negative and *AE* to rise, there is a drop in the fluxes to very small values of several units of #/(cm^2 sec *sr eV*) right close to the end of the day (Figure 4c). This dropout is seen for lower energies, too, from 4 to 15 keV (Figure 4e). After the dropout, the simultaneous increase of the observed fluxes is seen for all energies. This jump in the flux was from 2 orders of magnitude for the energies from 15 to 19.1 keV to 4 times for the energies from 39.7 to 50.7 keV. The increase was even more significant for lower energies, being about 3 orders of magnitude for the lowest energy of 4.81–5.74 keV and 2 orders of magnitude for the energies of 11.8–15 keV. After that there were two more drops and increases corresponding to IMF B_z decreases and peaks in *AE*, the lower the energy, the smaller the variations.

[33] Figures 4d and 4f present the modeled electron fluxes for the energy ranges as in Figures 4c and 4e obtained using IMPTAM by following the electron distribution from 10 R_E with *Tsyganenko and Mukai* [2003] boundary conditions to the AMC 12 orbit in the combination of the Tsyganenko T96 magnetic field and *Boyle et al.* [1997] electric field models. During the end of 28 November to the beginning of 29 November, in addition to the substorm activity seen in the *AE* index, variations are present in IMF B_y and B_z, solar wind velocity, number density, and dynamic pressure.

[34] The modeled electron fluxes show the variations for which the changes of model parameters are responsible (Figures 4d and 4f). During the quiet period on 28 November, there are not many variations seen in the modeled fluxes, and the values are similar to those for 25 November (see Figures 2d and 2f). At the end of the day on 28 November, there is a sharp increase of all fluxes at around 2200 UT followed by a decrease until about 00 UT on 29 November. This behavior corresponds to the observations (Figures 4c and 4e). The following peaks, which occurred at the beginning of 29 November, 0000–0200 UT, are not reproduced since they are associated with substorm activity.

[35] At about 0600 UT on 29 November the IMF B_z turned southward again but reached only –5 nT. During this time, the *AE* index started to increase with peak of 660 nT around 0900 UT. The satellite was on the dawnside moving toward dayside. A simultaneous increase of electron fluxes in all energy channels, more sharp for higher energies, was observed around 0700 UT. This increase was followed by another increase seen mainly for the highest energies, from 50 to 19 keV. For these energies, the increase was of about 2 orders of magnitude, from $2 \cdot 10^0$ #/(cm^2 sec *sr eV*) to $2 \cdot 10^2$ #/(cm^2 sec *sr eV*). No significant increase was observed for the electron fluxes with energies below 15 keV. This peak on 0600–1200 UT was not reproduced either, except for the flux drop at around 0600 UT, which corresponds to the observations. No significant variations were seen in solar wind and IMF parameters, which could have driven the models inside IMPTAM to reproduce the observed peak.

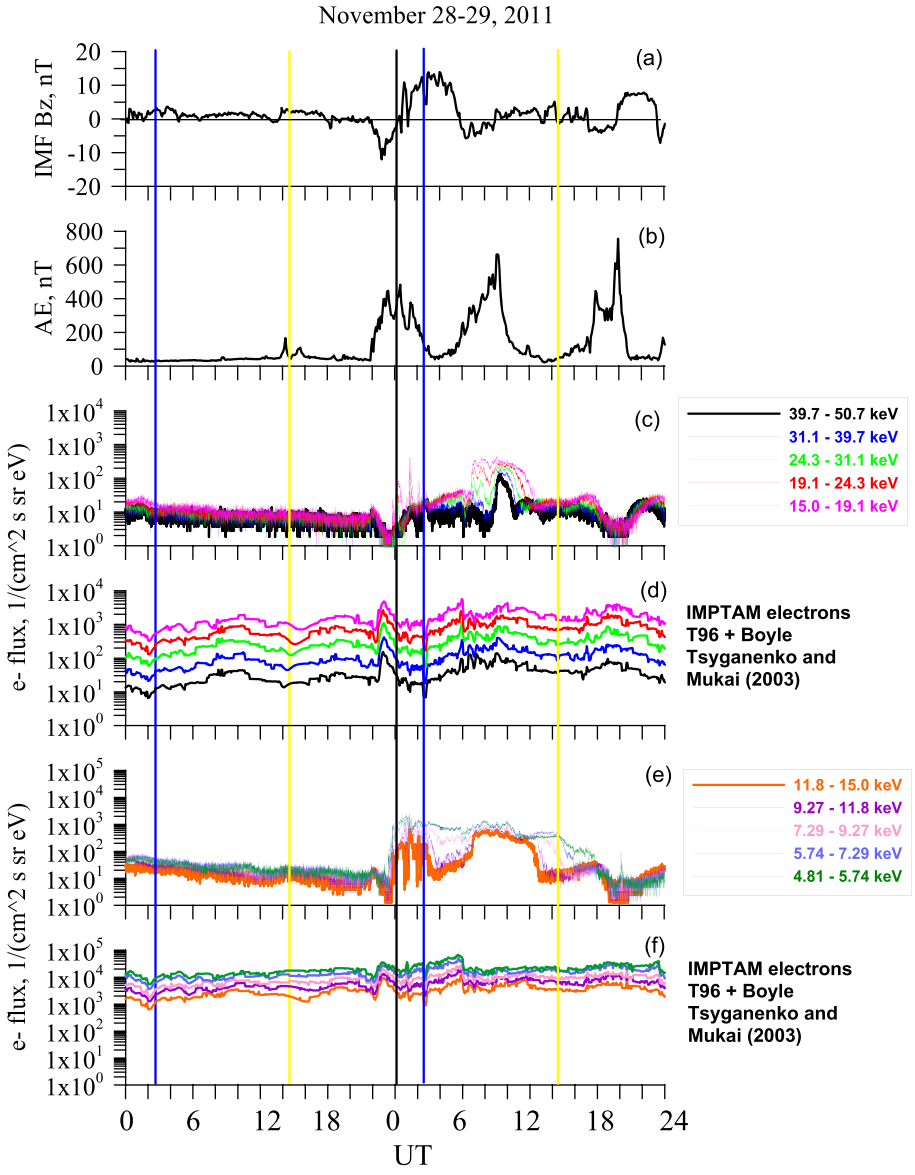

Figure 4. Similar as in Figure 2 but for 28–29 November 2011 event.

[36] The observed variations in the electron fluxes can be reproduced in IMPTAM by the changes in driving conditions for the modeled electrons, if the model parameters show changes big enough (for 29 November 2011 they were such that IMF B_z = –11 nT, V_{sw} = 530 km/s, P_{sw} = 6 nPa, *Kp* = 4, *AE* = 500 nT, *Dst* = –20 nT).

5.3. Representation of Substorm Activity

5.3.1. Substorm-Associated Impulsive Electric and Magnetic Fields

[37] In addition to the large-scale fields, transient fields associated with the dipolarization process in the magnetotail during substorm onset are included similarly as in *Ganushkina et al.* [2005, 2013]. In our study, we use the *Li et al.* [1998] model with modifications for pulse velocity introduced by *Sarris et al.* [2002] to represent the dipolarization process. The dipolarization was modeled as an earthward propagating electromagnetic pulse of localized radial and longitudinal extent. During this dipolarization process, the northward equatorial magnetic field increases due to a temporally and spatially varying westward electric field. The electric field is modeled as a time dependent Gaussian pulse with a purely azimuthal electric field component that

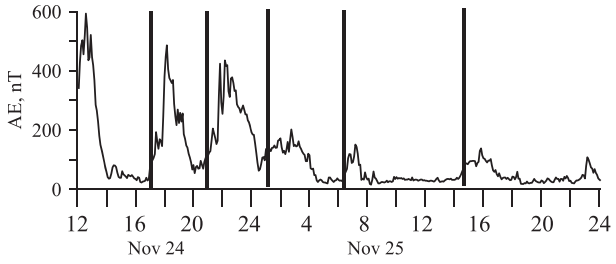

Figure 5. *AE* index for 24–25 November 2011 with times of substorm onsets marked by vertical lines.

Table 1. Times of Substorm Onsets, Corresponding Peak Magnitudes of *AE* Index, and Amplitudes E_0 of the Launched Pulses for 24–25 November 2011

UT	*AE* Peak (nT)	E_0 (mV/m)
24 November 2011		
1700	500	3.9
2115	430	3.4
25 November 2011		
0100	200	1.6
0610	150	1.2
1430	140	1.1

propagates radially inward at a decreasing velocity, decreases away from midnight, and is partially reflected near the plasmapause. The earthward propagation speed decreased as the pulse moved inward to mimic the breaking of the flows. According to *Li et al.* [1998], each pulse lasts about 10 min.

[38] In the spherical coordinate system (r, θ, ϕ), where $r = 0$ at the center of the Earth, $\theta = 0$ defines the equatorial plane, and $\phi = 0$ is at local noon (positive eastward), the electric field is given by

$$\mathbf{E}_\phi = -\hat{e}_\phi E_0 (1 + c_1 \cos(\phi - \phi_0))^p \exp(-\xi^2) \quad (7)$$

where $\xi = [r - r_i + v(r)(t - t_a)]/d$ determines the location of the maximum value of the pulse, $v(r) = a + br$ is the pulse front velocity as a function of radial distance r, d is the width of the pulse, $c_1 (> 0)$ and $p (> 0)$ describe the local time dependence of the electric field amplitude, which is largest at ϕ_0, $t_a = (c_2/v_a)(1 - cos(\phi - \phi_0))$, represents the delay of the pulse from ϕ_0 to other local times, c_2 determines the magnitude of the delay, v_a is the longitudinal speed of the pulse (assumed constant),and r_i is a parameter in the simulation that determines the arrival time of the pulse.

[39] We launch a pulse at each substorm onset during the period of a modeled storm. We show the results for 25 November 2011 here for detailed discussion, since other time periods had similar features and are not shown here. The substorm onsets and the peaks have been automatically detected by a routine that locates steep gradients and local maxima in the *AL* and *AE* indices [*Amariutei and Ganushkina*, 2012]. The amplitude of the pulse has been scaled accordingly to the amplitudes of the *AE* peaks. Figure 5 shows the *AE* index for the 24–25 November 2011 modeled event with times of substorm onsets marked by vertical lines and, Table 1 presents the times of substorm onsets, corresponding peak magnitudes of the *AE* index, and amplitudes E_0 of the launched pulses.

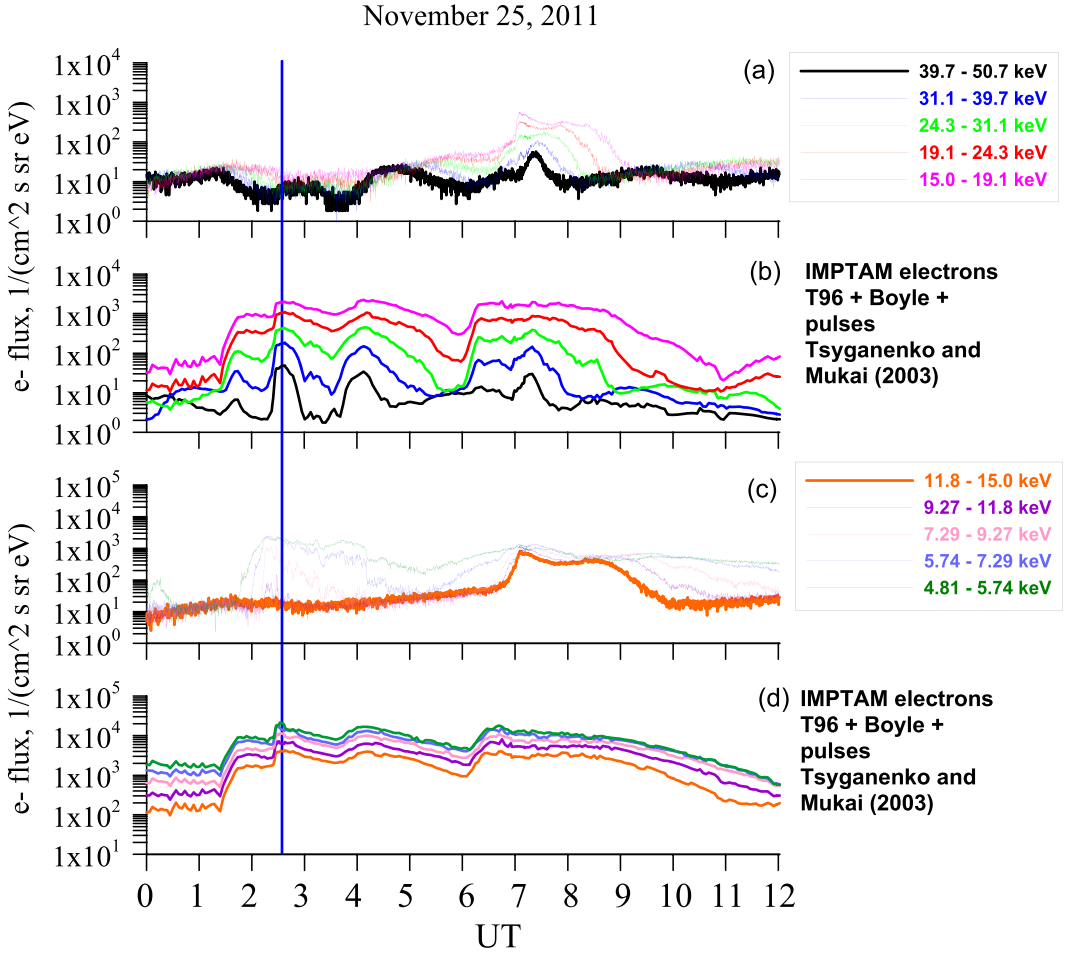

Figure 6. Influence of substorm activity: The electron fluxes (a and c) observed by the AMC 12 CEASE II ESA instrument and (b and d) modeled by IMPTAM at geostationary orbit during 25 November 2011, 0000–1200 UT, in 10 energy channels, similar as in Figure 2.

5.3.2. Substorm-Related Effects on Electron Fluxes on 25 November 2011

[40] As was shown above, the variations of model parameters in IMPTAM are so small for the rather quiet event on 24–30 November 2011 that the substorm activity seen in the *AE* index can be responsible for the observed variations in low-energy electron fluxes. We focus on the modeling of 24–25 November 2011 period, and in addition to the large-scale electric and magnetic fields, we launched several electromagnetic pulses at substorm onsets determined as sharp increases in the *AE* index (Figure 5) with amplitudes given in Table 1.

[41] Figure 6 presents the results by comparing electron fluxes observed (a and c) by the AMC 12 CEASE II ESA instrument at geostationary orbit and modeled ones (b and d) during 12 h of 25 November 2011. The addition of substorm-associated pulses did change the pattern of modeled electron fluxes. The observed peaks were mostly captured but not with the correct timing. For higher-energy fluxes (Figure 6b), there is an increase around 0130–0300 UT, when the satellite was near midnight. The modeled fluxes showed a rise of about 1.5 orders of magnitude. This increase was due to the pulses coming at the end of 24 November to the beginning of 25 November. Since the pulses are launched on the nightside, the modeled fluxes experience their influence very clearly. The observed fluxes did not show the increase as big as seen in the modeled fluxes. At the same time, there is an observed peak in the energies higher than 30 keV around 0500 UT, and it was reproduced by the model. The more pronounced peak around 0700–0800 UT was also captured with similar dependence of a more narrow peak for higher energies (>30 keV) and a broader peak for smaller energies (15–30 keV), as observed.

[42] For lower energies (Figure 6d), the modeled fluxes show the increases which correspond to the observed ones but these increases are seen for all energy ranges. The increase, which is seen around 0130 UT, is captured by the model but with fluxes higher by an order of magnitude. Observations show that the increase happens only for the energies smaller than 11.8 keV. Another increase with broad peak which corresponds to the observations is seen around 0600–0630 UT. This later increase corresponds to the satellite position on the dawnside and is due to the particles accelerated by the pulse launched around 0600 UT (Figure 5).

[43] The modeled fluxes with addition of pulses are plotted in Figure 3, similar as for the observed fluxes and fluxes modeled without addition of pulses, as fluxes before the *AE* peak (red lines) and as fluxes at the *AE* peak (dashed red lines) for the (a) first and (b) second peaks. The modeled fluxes are elevated before the first *AE* peak (Figure 3a) due to the presence of pulses on 24 November, and they are more close to the observed fluxes at the *AE* peak. At the first *AE* peak the modeled fluxes show the increase in all energies, even for 15–50 keV electrons which, as it is observed, do not increase. Before the second *AE* peak (Figure 3b), the modeled fluxes are very close to the observed ones for > 25 keV electrons. At the *AE* peak modeled fluxes for all the energies are increased by an order of magnitude.

[44] The variations of the observed fluxes during this nonstorm period are due to substorm activity. The substorm-associated increases in the observed fluxes can be captured when substorm-associated electromagnetic fields are taken into account.

6. Discussion

[45] The analysis of measured electron fluxes in 10 energy ranges (from 5 to 50 keV) on board the AMC 12 geostationary spacecraft by the CEASE II ESA instrument during quiet event, and the output of the IMPTAM modeling has revealed very interesting results. The variations of fluxes for electrons in 10 energy ranges as observed by the CEASE II ESA instrument were present even though no significant, storm-related variations were seen in the solar wind and IMF parameters. The peaks were clearly associated with substorm activity as seen in the *AE* index. The behavior of the fluxes depends on the electron energy. If the satellite is near midnight (Figure 2) when a substorm is developing (as seen in *AE*), then the corresponding peak is seen in the fluxes of electrons with lower energies starting only from the channel of 9.27–11.8 keV and down to the channels with lowest energies of 4.81–5.74 keV. No peaks are seen for the energies above 11.8 keV.

[46] The peaks in all energy channels are seen when the satellite is on the dawnside, moving toward noon, as it happened on 25 November (Figure 2), 27 November (data not shown), and 29 November (Figure 4). With the growth of the *AE* index, the fluxes of all energy channels show the simultaneous increase. The fluxes with energies below 15 keV stay increased until the *AE* index comes back to undisturbed values. The fluxes with energies above 19 keV decrease while *AE* index increases and then show a peak again at the time of *AE* maximum. Especially, it is clearly observed for the energy channels of 31.1–39.7 keV and 39.7–50.7 keV.

[47] Particle energy and configuration of electric and magnetic fields which particle moves in determine, among the others factors, its access to geostationary orbit [*Korth et al.*, 1999]. The Alfvén layers, i.e., the boundary between open and closed drift paths, for 5–50 keV charged particles intersect geosynchronous orbit at locations that depend on them. Lower energy particles, for which the Alfvén layers are located closer to the Earth, experience a sudden increase in flux, while higher-energy particles remain constant, possibly because the particles cannot access the observing location. It can be clearly seen in Figures 2c and 2e, where increase in fluxes were present only for electrons with energies below 11.8 keV during first increase in the *AE* index. Changes in the electric field pattern may significantly modify the access to a given location.

[48] We must stress once again that the absolute flux values presented here may not be correct due to uncertainties in the sensor geometric factors. We compare the observed and modeled fluxes keeping this in mind. As a result of the comparison of modeled fluxes to the CEASE II ESA observations, we found that the observed peaks cannot be reproduced (Figures 2, 4) by the set of background magnetic and electric field models and boundary conditions used in IMPTAM for this event. IMPTAM is driven by the variations in the solar wind and IMF via the dependence of the background magnetic and electric field models and boundary conditions on the solar wind number density, velocity, dynamics pressure, IMF components, and *Dst* index. If no significant variations are seen in these parameters, no

observed peaks can be represented. The 24–30 November 2011 event was quiet, nonstorm (Figure 1), with no variations in the solar wind and IMF parameters which could have driven IMPTAM. At the same time, the observed fluxes showed increases and peaks during this quiet period.

[49] The averaged model fluxes were found to be different from the observed ones. The smaller the electron energy, the larger the flux difference, reaching 3 orders of magnitude for 4.81–5.74 keV electrons, 2 orders of magnitude for 15–19.1 keV electrons, and being close for 37.9–50.7 keV electrons. As was discussed in *Ganushkina et al.* [2013], the difference cannot be explained by inaccuracy of the field models, since it was present for all combinations of electric and magnetic field models used in the study by *Ganushkina et al.* [2013]. Apart from the possibility of incorrect values for the measured fluxes mentioned above, one additional explanation is that the boundary conditions we used at 10 R_E were adapted from the empirical model derived from Geotail data by *Tsyganenko and Mukai* [2003] for ions. We used the same number density as for ions and for electron temperature we just set Te/Ti = 0.2. According to recent studies based on Geotail data analysis [*Wang et al.*, 2011], the ratio Te/Ti can vary during disturbed conditions. Furthermore, there was no MLT dependence in the kappa distribution with n and T parameters from the *Tsyganenko and Mukai* [2003] model, which is also not the case according to the observations [*Wang et al.*, 2011]. Thus, the model we used for boundary conditions has a number of limitations. However, it is currently the best analytical model that can be used for time-dependent boundary conditions at 10 R_E in the plasma sheet. The use of more accurate analytical models for boundary fluxes may significantly improve the simulation results.

[50] Another important issue is the representation of the loss processes for modeled electrons to the atmosphere due to the resonant pitch-angle scattering by chorus waves. Chorus waves are excited by the anisotropy of low-energy electrons, which are injected into the inner magnetosphere during the periods of enhanced convection [*Meredith et al.*, 2001; *Lyons et al.*, 2005]. Interactions with chorus waves lead to electron pitch angle scattering into the loss cone, where they are removed within a quarter bounce time [*Horne and Thorne*, 2003]. Our modeling included loss processes similar to *Shprits et al.* [2007] and *Chen et al.* [2005]. Introducing the loss processes due to wave-particle interactions in a proper way is important for low-energy electrons and will be part of our future study.

[51] Since no variations were observed in the solar wind and IMF parameters for, for example, 25 November 2011 (Figure 2), but the peaks were present in the observed electron fluxes, they can be associated with substorm activity seen in the *AE* index. The large-scale background electric and magnetic fields used in IMPTAM do not have the effect of substorm variations; therefore, the peaks were not reproduced by IMPTAM. The substorm-associated electromagnetic fields play a significant role in the electron transport and acceleration from the plasma sheet to the inner magnetosphere [*Ganushkina et al.*, 2013], and they must be taken into account when modeling the electron population. As can be seen in Figure 6, the increases in the modeled fluxes correspond to the pulses launched at about those times (Figure 5 and Table 1).

[52] Other studies have used a similar representation of electromagnetic pulses by *Li et al.* [1998] or *Sarris et al.* [2002], and good agreement with the observed dispersionless electron injections at geostationary orbit was obtained [*Ingraham et al.*, 2001; *Li et al.*, 2003; *Mithaiwala and Horton*, 2005; *Liu et al.*, 2009]. Isolated substorms during nonstorm times can be very different from storm-time substorms [*Pulkkinen et al.*, 2005]. Modifications are needed for the pulse model. As was mentioned in *Ganushkina et al.* [2013], the linear dependence of the pulse's velocity on R_E, the arrival time of the pulse, the azimuthal extent, and the impact location [*Sarris and Li*, 2005] must be changed to fit observations [*Reeves et al.*, 1996; *Ohtani*, 1998; *Sergeev et al.*, 1998]. Other possible reasons for the discrepancies between the modeled fluxes with pulses and the observed ones may be that (1) the injection did not start at the start radial distance and/or time of the model pulse, (2) the injection did not happen at the modeled pulse peak at midnight but at other MLTs, (3) the electric field amplitude is not directly proportional to the *AE* index used for simulations, and (4) the width of the pulse is different from the model settings. All of these are parameters that can be fine tuned and perhaps parameterized with empirically based functional forms.

[53] Since the absolute values of measured fluxes may not be relevant for the direct comparison with the modeled fluxes, Figure 3 can be analyzed in terms of the slopes of the presented flux-energy spectra before and at *AE* peaks. It should be also mentioned that similar behavior of the observed and modeled fluxes was obtained for 27 November and 28–29 November (now shown). The model results with pulses clearly correspond to the shift of electrons with all energies inward and their energization due to action of pulses. For the second *AE* peak, the observed fluxes show a similar trend in the slopes suggesting that it was the action of a substorm injection, which pushed the electrons and energized them. For the first peak, the situation is not so clear. This can mean that the injection was weak and that the gradient-curvature drift turned the higher-energy electrons away from reaching the geosynchronous orbit. On the other hand, the pulse can be eastward of the satellite, and so only the lowest-energy electrons, that penetrate the deepest, were seen by the AMC 12, while the higher-energy electrons had already started their gradient-curvature drift eastward and missed the satellite. In any case, the clear increase in all 10 energy channels simultaneously is observed when the satellite was at dawn with an *AE* peak present at that time.

7. Conclusions

[54] We investigated the low-energy (5–50 keV) electron transport and acceleration from the plasma sheet to geostationary orbit. These fluxes constitute the low-energy part of the seed population for the high-energy MeV particles and can also provide energy for chorus waves. Moreover, energetic electrons with energies less than about 100 keV are responsible for hazardous space weather phenomena such as surface charging. We specifically studied the role of large-scale convection and influence of the substorm-associated electromagnetic fields on the modeled electron fluxes at geostationary orbit. We used the Inner Magnetosphere Particle Transport and Acceleration model (IMPTAM) [*Ganushkina*

et al., 2001, 2005, 2006, 2012] for electrons [*Ganushkina et al.*, 2013] with the boundary at 10 R_E, where we set boundary conditions for the electrons based on Tsyganenko and Mukai [*Tsyganenko and Mukai*, 2003] model. We modeled one rather quiet, nonstorm event on 24–30 November 2011, when the presence of isolated substorms was seen in *AE* index. The output of the IMPTAM modeling is compared to the observed electron fluxes in 10 energy ranges (5–50 keV) measured on board the AMC 12 spacecraft by the CEASE II ESA instrument. We presented the data and modeling results for 25 November and 28–29 November 2011 time intervals.

[55] Keeping the points discussed above in mind, the conclusions are as follows:

[56] 1. The variations of fluxes for low-energy electrons (5–50 keV) as observed by CEASE II ESA instrument onboard AMC 12 satellite during nonstorm period are due to substorm activity. The behavior of the fluxes depends on the electron energy. The increase of electron fluxes corresponding to the increase in the *AE* index is observed only for energies below 11.8 keV, when the satellite was near midnight. When the satellite was on the dawnside, moving toward noon, the fluxes with all the energies show the simultaneous increase with the growth of the *AE* index. The fluxes with energies below 15 keV stay increased until the *AE* index comes back to undisturbed values. The fluxes with energies above 19 keV decrease while *AE* index increases and then show a peak again at the time of *AE* maximum.

[57] 2. IMPTAM driven by the parameters such as IMF B_y and B_z, solar wind velocity, number density and dynamic pressure, and Dst index is not able to reproduce the observed peaks in the electron fluxes, when no significant variations are present in those parameters. No simple drifts in the large-scale electric and magnetic fields can be applied.

[58] 3. The observed variations in the electron fluxes can be reproduced if the model parameters show changes big enough (for 29 November 2001 IMF B_z = –11 nT, V_{sw} = 530 km/s, P_{sw} = 6 nPa, Kp = 4, AE = 500 nT, Dst = –20 nT).

[59] 4. The substorm-associated increases in the observed fluxes can be captured when substorm-associated electromagnetic fields are taken into account. Modifications of the pulse model by *Sarris et al.* [2002] used here are needed, especially related to the pulse front velocity and arrival time.

[60] The ability to explain and, in the future, to predict the variations of low-energy electrons at any location in the inner magnetosphere is crucial for dealing with surface charging of satellites. As it was shown, even during quiet periods with moderate substorm activity, a clear increase in the spacecraft potential magnitudes was detected with a corresponding increase in low-energy electron fluxes.

[61] **Acknowledgments.** We thank OMNIWEB data center for IMF and solar wind parameter data, World Data Center C2 for Geomagnetism, Kyoto, for the provisional *AE*, *Kp*, and *SYM – H* indices data. The research leading to these results has received funding from the European Union Seventh Framework Programme (FP7/2007–2013) under grant agreement No 262468. N. Ganushkina gratefully acknowledges the support of part of this work by NASA and NSF grants. Work of N. Ganushkina was also partly supported by the Academy of Finland. The authors also thank the International Space Science Institute (ISSI) in Bern, Switzerland, for its support of an international team on "The Earth's Radiation Belts: Physical Processes and Dynamic Modeling".

[62] Masaki Fujimoto thanks Norma Crosby and Haje Korth for their assistance in evaluating this paper.

References

Aggson, T. L., J. P. Heppner, and N. C. Maynard (1983), Observations of large magnetospheric electric fields during the onset phase of a substorm, *J. Geophys. Res.*, *88*(A5), 3981–3990, doi:10.1029/JA088iA05p03981.

Amariutei, O. A., and N. Y. Ganushkina (2012), On the prediction of the auroral westward electrojet index, *Ann. Geophys.*, *30*, 841–847.

Bame, S. J., D. J. McComas, M. F. Thomsen, B. L. Barraclough, R. C. Elphic, J. P. Glore, J. T. Gosling, J. C. Chavez, E. P. Evans, and F. J. Wymer (1993), Magnetospheric plasma analyzer for spacecraft with constrained resources, *Rev. Sci. Instr.*, *64*, 1026–1033.

Bogorad, A., C. Bowman, A. Dennis, J. Beck, D. Lang, R. Herschitz, M. Buehler, B. Blaes, and D. Martin (1995), Integrated environmental monitoring system for spacecraft, *IEEE Trans. Nucl. Sci.*, *42*, 2051–2057.

Boonsiriseth, A., R. M. Thorne, G. Lu, V. K. Jordanova, M. F. Thomsen, D. M. Ober, and A. J. Ridley (2001), A semiempirical equatorial mapping of AMIE convection electric potentials (MACEP) for the January 10, 1997, magnetic storm, *J. Geophys. Res.*, *106*(A7), 12,903–12,918, doi:10.1029/1999JA000332.

Borovsky, J. E., M. F. Thomsen, R. C. Elphic, T. E. Cayton, and D. J. McComas (1998), The transport of plasma sheet material from the distant tail to geosynchronous orbit, *J. Geophys. Res.*, *103*, 20,297–20,331.

Boyle, C., P. Reiff, and M. Hairston (1997), Empirical polar cap potentials, *J. Geophys. Res.*, *102*(A1), 111–125.

Brautigam, D. H., and J. M. Albert (2000), Radial diffusion analysis of outer radiation belt electrons during the 9 October 1990 magnetic storm, *J. Geophys. Res.*, *105*, 291–309.

Cattell, C. A., and F. S. Mozer (1984), Substorm electric fields in the earth's magnetotail, in *Magnetic Reconnection in Space and Laboratory Plasmas, Geophys. Monogr. Ser.,* vol. 30, edited by E. W. Hones Jr., pp. 208–215, AGU, Washington, D. C.

Chen, M. W., M. Schulz, G. Lu, and L. R. Lyons (2003), Quasi-steady drift paths in a model magnetosphere with AMIE electric field: Implications for ring current formation, *J. Geophys. Res.*, *108*(A5), 1180, doi:10.1029/2002JA009584.

Chen, M. W., M. Schulz, P. C. Anderson, G. Lu, G. Germany, and M. Wüest (2005), Storm time distributions of diffuse auroral electron energy and X-ray flux: Comparison of drift-loss simulations with observations, *J. Geophys. Res.*, *110*, A03210, doi:10.1029/2004JA010725.

Chen, Y., G. D. Reeves, and R. H. W. Friedel (2007), The energization of relativistic electrons in the outer Van Allen radiation belt, *Nat. Phys.*, *3*, 614–617, doi:10.1038/nphys655.

Davis, V. A., M. J. Mandell, and M. F. Thomsen (2008), Representation of the measured geosynchronous plasma environment in spacecraft charging calculations, *J. Geophys. Res.*, *113*, A10204, doi:10.1029/2008JA013116.

Degtyarev, V. I., G. V. Popov, and S. S. Sheshukov (1990), Modelling the dynamics of fluxes of electrons with energies 30–300 keV in geostationary orbit, *Geomag. Aeron.*, *30*, 866–868.

Denton, M. H., M. F. Thomsen, H. Korth, S. Lynch, J. C. Zhang, and M. W. Liemohn (2005), Bulk plasma properties at geosynchronous orbit, *J. Geophys. Res.*, *110*, A07223, doi:10.1029/2004JA010861.

Dichter, B. K., J. 0. McGarity, M. R. Oberhardt, V. T. Jordanov, D. J. Sperry, A. C. Huber, J. A. Pantazis, E. G. Mullen, G. Ginet, and M. S. Gussenhoven (1998), Compact Environmental Anomaly Sensor (CEASE): A novel spacecraft instrument for in situ measurements of environmental conditions, *IEEE Trans. Nucl. Sci.*, *45*, 2758–2764.

Elkington, S. R., M. Wiltberger, A. A. Chan, and D. N. Baker (2004), Physical models of the geospace radiation environment, *J. Atmos. Sol. Terr. Phys.*, *66*, 1371–1387.

Fälthammar, C.-G. (1965), Effects of time-dependent electric fields on geomagnetically trapped radiation, *J. Geophys. Res.*, *70*, 2503–2516.

Frezet, M., J. P. Granger, L. Levy, and J. Hamelin (1988), Assessment of charging behaviour of Meteosat spacecraft in geosynchronous environment, ONERA Paper 233 248 presented at CERT, paper presented at 4th International Conference on Spacecraft Materials in Space Environment, ONERA Toulouse Research Center, Toulouse, France.

Friedel, R. H. W., H. Korth, M. G. Henderson, M. E. Thomsen, and J. D. Scudder (2001), Plasma sheet access to the inner magnetosphere, *J. Geophys. Res.*, *106*, 5845–5858.

Fok, M.-C., T. E. Moore, and W. N. Spjeldvik (2001), Rapid enhancement of radiation belt electron fluxes due to substorm dipolarization of the geomagnetic field, *J. Geophys. Res.*, *106*(A3), 3873–3882, doi:10.1029/2000JA000150.

Ganushkina, N. Y., T. I. Pulkkinen, V. F. Bashkirov, D. N. Baker, and X. Li (2001), Formation of intense nose structures, *Geophys. Res. Lett.*, *28*(3), 491–494.

Ganushkina, N. Y., T. I. Pulkkinen, and T. Fritz (2005), Role of substorm-associated impulsive electric fields in the ring current development during storms, *Ann. Geophys.*, *23*, 579–591.

Ganushkina, N. Y., T. I. Pulkkinen, M. Liemohn, and A. Milillo (2006), Evolution of the proton ring current energy distribution during April 21–25, 2001 storm, *J. Geophys. Res.*, *111*, A11S08, doi:10.1029/2006JA011609.

Ganushkina, N. Y., M. W. Liemohn, and T. I. Pulkkinen (2012), Storm-time ring current: Model-dependent results, *Ann. Geophys.*, *30*, 177–202.

Ganushkina, N. Y., O. Amariutei, Y. Y. Shpritz, and M. Liemohn (2013), Transport of the plasma sheet electrons to the geostationary distances, *J. Geophys. Res. Space Physics*, *118*, 82–98, doi:10.1029/2012JA017923.

Garrett, H. B. (1981), The charging of spacecraft surfaces, *Rev. Geophys.*, *19*(4), 577–616, doi:10.1029/RG019i004p00577.

Grafodatskiy, O. S., V. I. Degtyarev, A. G. Kozlov, V. I. Lazarev, O. I. Platonov, G. V. Popov, and M. V. Teltsov (1987), Relationship between characteristics of low-energy electrons and geomagnetic disturbance in geostationary orbit, *Geomag. Aeron.*, *27*, 494–496.

Hardy, D. A., D. M. Walton, A. D. Johnstone, M. F. Smith, M. P. Gough, A. Huber, J. Pantazis, and R. Burkhardt (1993), Low Energy Plasma Analyzer, *IEEE Trans. Nucl. Sci.*, *40*, 246–251.

Hoeber, C. F., E. A. Robertson, I. Katz, V. A. Davis, and D. B. Snyder (1998), Solar array augmented electrostatic discharge in GEO, AIAA Paper 98–1401, paper presented at 17th AIAA International Communications Spacecraft Systems Conference and Exhibit, Am. Inst. of Aeron, and Astron., Yokohama, Japan.

Horne, R. B., and R. M. Thorne (2003), Relativistic electron acceleration and precipitation during resonant interactions with whistler-mode chorus, *Geophys. Res. Lett.*, *30*(10), 1527, doi:10.1029/2003GL016973.

Horne, R. B., et al. (2005), Wave acceleration of electrons in the Van Allen radiation belts, *Nature*, *437*, 227–230, doi:10.1038/nature03939.

Horne, R. B., et al. (2013), Forecasting the Earth's radiation belts and modelling solar energetic particle events: Recent results from SPACECAST, *J. Space Weather Space Clim.*, *3*, A20, doi:10.1051/swsc/2013042.

Ingraham, J. C., T. E. Cayton, R. D. Belian, R. A. Christensen, R. H. W. Friedel, M. M. Meier, G. D. Reeves, and M. Tuszewski (2001), Substorm injection of relativistic electrons to geosynchronous orbit during the great magnetic storm of March 24, 1991, *J. Geophys. Res.*, *106*, 25,759–25,776.

Kaufmann, R. L., W. R. Paterson, and L. A. Frank (2005), Relationships between the ion flow speed, magnetic flux transport rate, and other plasma sheet parameters, *J. Geophys. Res.*, *110*, A09216, doi:10.1029/2005JA011068.

Kennel, C. F., and H. E. Petschek (1966), Limit on stable trapped particle fluxes, *J. Geophys. Res.*, *71*(1), 1–28, doi:10.1029/JZ071i001p00001.

Kennel, C. F., and R. M. Thorne (1967), Unstable growth of unducted whistlers propagating at an angle to the geomagnetic field, *J. Geophys. Res.*, *72*(3), 871–878, doi:10.1029/JZ072i003p00871.

Khazanov, G. V., M. W. Liemohn, T. S. Newman, M.-C. Fok, and A. J. Ridley (2004a), Magnetospheric convection electric field dynamics and stormtime particle energization: Case study of the magnetic storm of 4 May 1998, *Ann. Geophys.*, *22*, 497–510.

Khazanov, G. V., M. W. Liemohn, M.-C. Fok, T. S. Newman, and A. J. Ridley (2004b), Stormtime particle energization with AMIE potentials, *J. Geophys. Res.*, *109*, A05209, doi:10.1029/2003JA010186.

Koons, H. C., J. E. Mazur, R. S. Selesnick, J. B. Blake, J. F. Fennell, J. L. Roeder, and P. C. Anderson (1999), The impact of the space environment on space systems, *Aerospace Rep. TR-99 (1670)-1*, Aerospace Corp., El Segundo, Calif.

Korth, H., M. F. Thomsen, J. E. Borovsky, and D. J. McComas (1999), Plasma sheet access to geosynchronous orbit, *J. Geophys. Res.*, *104*, 25,047–25,061.

Kozelova, T. V., L. L. Lazutin, B. V. Kozelov, N. Meredith, and M. A. Danielides (2006), Alternating bursts of low energy ions and electrons near the substorm onset, *Ann. Geophys.*, *24*, 1957–1968.

Kurita, S., et al. (2011), Transport and loss of the inner plasma sheet electrons: THEMIS observations, *J. Geophys. Res.*, *116*, A03201, doi:10.1029/2010JA015975.

Lejosne, S., D. Boscher, V. Maget, and G. Rolland (2013), Deriving electromagnetic radial diffusion coefficients of radiation belt equatorial particles for different levels of magnetic activity based on magnetic field measurements at geostationary orbit, *J. Geophys. Res. Space Physics*, *118*, 3147–3156, doi:10.1002/jgra.50361.

Li, X., D. N. Baker, M. Temerin, G. D. Reeves, and R. D. Belian (1998), Simulation of dispersionless injections and drift echoes of energetic electrons associated with substorms, *Geophys. Res. Lett.*, *25*, 3763–3766.

Li, X., T. E. Sarris, D. N. Baker, W. K. Peterson, and H. J. Singer (2003), Simulation of energetic particle injections associated with a substorm on August 27, 2001, *Geophys. Res. Lett.*, *30*, 1004, doi:10.1029/2002GL015967.

Li, W., R. M. Thorne, N. P. Meredith, R. B. Horne, J. Bortnik, Y. Y. Shprits, and B. Ni (2008), Evaluation of whistler-mode chorus amplification during an injection event observed on CRRES, *J. Geophys. Res.*, *113*, A09210, doi:10.1029/2008JA013129.

Li, W., R. Thorne, J. Bortnik, R. McPherron, Y. Nishimura, V. Angelopoulos, and I. G. Richardson (2012), Evolution of chorus waves and their source electrons during storms driven by corotating interaction regions, *J. Geophys. Res.*, *117*, A08209, doi:10.1029/2012JA017797.

Liu, W. L., X. Li, T. Sarris, C. Cully, R. Ergun, V. Angelopoulos, D. Larson, A. Keiling, K. H. Glassmeier, and H. U. Auster (2009), Observation and modeling of the injection observed by THEMIS and LANL satellites during the 23 March 2007 substorm event, *J. Geophys. Res.*, *114*, A00C18, doi:10.1029/2008JA013498.

Lyons, L. R., D.-Y. Lee, R. M. Thorne, R. B. Horne, and A. J. Smith (2005), Solar wind-magnetosphere coupling leading to relativistic electron energization during high-speed streams, *J. Geophys. Res.*, *110*, A11202, doi:10.1029/2005JA011254.

Maynard, N. C., W. J. Burke, E. M. Basinska, G. M. Erickson, W. J. Hughes, H. J. Singer, A. G. Yahnin, D. A. Hardy, and F. S. Mozer (1996), Dynamics of the inner magnetosphere near times of substorm onsets, *J. Geophys. Res.*, *101*(A4), 7705–7736, doi:10.1029/95JA03856.

Meredith, N. P., R. B. Horne, and R. R. Anderson (2001), Substorm dependence of chorus amplitudes: Implications for the acceleration of electrons to relativistic energies, *J. Geophys. Res.*, *106*, 13,165–13,178.

Mithaiwala, M. J., and W. Horton (2005), Substorm injections produce sufficient electron energization to account for MeV flux enhancements following some storms, *J. Geophys. Res.*, *110*, A07224, doi:10.1029/2004JA010511.

Miyoshi, Y. S., V. K. Jordanova, A. Morioka, M. F. Thomsen, G. D. Reeves, D. S. Evans, and J. C. Green (2006), Observations and modeling of energetic electron dynamics during the October 2001 storm, *J. Geophys. Res.*, *111*, A11S02, doi:10.1029/2005JA011351.

Ohtani, S. (1998), Earthward expansion of tail current disruption: Dual-satellite study, *J. Geophys. Res.*, *103*(A4), 6815–6825, doi:10.1029/98JA00013.

Pulkkinen, T. I., N. Y. Ganushkina, E. Donovan, X. Li, G. D. Reeves, C. T. Russell, H. J. Singer, and J. A. Slavin (2005), Storm-substorm coupling during 16 Hours of Dst steadily at 150 nT, in *The Inner Magnetosphere: Physics and Modeling*, edited by T. I. Pulkkinen, N. A. Tsyganenko, and R. H. W. Friedel, pp. 155–161, AGU, Washington, D. C.

Purvis, C. K., H. B. Garrett, A. C. Whittlesey, and N. J. Stevens (1984), Design guidelines for assessing and controlling spacecraft charging effects, *NASA Tech. Rep.*, NASA-TR 2361.

Reeves, G. D., M. G. Henderson, P. S. McLachlan, R. D. Belian, R. H. W. Friedel, and A. Korth (1996), Radial propagation of substorm injections, Proceedings of the 3rd International Conference on Substorms, Versailles, France.

Roederer, J. G. (1970), *Dynamics of Geomagnetically Trapped Radiation*, Springer-Verlag, New York.

Rowland, D. E., and J. R. Wygant (1998), Dependence of the large-scale, inner magnetospheric electric field on geomagnetic activity, *J. Geophys. Res.*, *103*(A7), 14,959–14,964, doi:10.1029/97JA03524.

Sarris, T. E., and X. Li (2005), Evolution of the dispersionless injection boundary associated with substorms, *Ann. Geophys.*, *23*, 877–884.

Sarris, T. E, X. Li, N. Tsaggas, and N. Paschalidis (2002), Modeling energetic particle injections in dynamic pulse fields with varying propagation speeds, *J. Geophys. Res.*, *107*, 1033, doi:10.1029/2001JA900166.

Schulz, M., and L. Lanzerotti (1974), *Particle Diffusion in the Radiation Belts*, Springer, New York.

Scudder, J., et al. (1995), Hydra: A 3-dimensional electron and ion hot plasma instrument for the Polar spacecraft of the GGS mission, *Space Sci. Rev.*, *71*, 459–495.

Sergeev, V. A., M. A. Shukhtina, R. Rasinkangas, A. Korth, G. D. Reeves, H. J. Singer, M. F. Thomsen, and L. I. Vagina (1998), Event study of deep energetic particle injections during substorm, *J. Geophys. Res.*, *103*(A5), 9217–9234, doi:10.1029/97JA03686.

Shprits, Y. Y., and R. M. Thorne (2004), Time dependent radial diffusion modeling of relativistic electrons with realistic loss rates, *Geophys. Res. Lett.*, *31*, L08805, doi:10.1029/2004GL019591.

Shprits, Y. Y., N. P. Meredith, and R. M. Thorne (2007), Parameterization of radiation belt electron loss timescales due to interactions with chorus waves, *Geophys. Res. Lett.*, *34*, L11110, doi:10.1029/2006GL029050.

Sicard-Piet, A., S. Bourdarie, D. Boscher, R. H. W. Friedel, M. Thomsen, T. Goka, H. Matsumoto, and H. Koshiishi (2008), A new international geostationary electron model: IGE-2006, from 1 keV to 5.2 MeV, *Space Weather*, *6*, S07003, doi:10.1029/2007SW000368.

Stern, D. (1975), The motion of a proton in the equatorial magnetosphere, *J. Geophys. Res.*, *80*(4), 595–599.

Thomsen, M. F., H. Korth, and R. C. Elphic (2002), Upper cutoff energy of the electron plasma sheet as a measure of magnetospheric convection strength, *J. Geophys. Res.*, *107*, 1331, doi:10.1029/2001JA000148.

Tsurutani, B. T., and E. J. Smith (1974), Postmidnight chorus: A substorm phenomenon, *J. Geophys. Res.*, *79*(1), 118–127, doi:10.1029/JA079i001p00118.

Tsyganenko, N. A. (1995), Modeling the Earth's magnetospheric magnetic field confined within a realistic magnetopause, *J. Geophys. Res.*, *100*, 5599–5612.

Tsyganenko, N. A., and T. Mukai (2003), Tail plasma sheet models derived from Geotail particle data, *J. Geophys. Res.*, *108*(A3), 1136, doi:10.1029/2002JA009707.

Tu, J.-N., K. Tsuruda, H. Hayakawa, A. Matsuoka, T. Mukai, I. Nagano, and S. Yagitani (2000), Statistical nature of impulsive electric fields associated with fast ion flow in the near-Earth plasma sheet, *J. Geophys. Res.*, *105*(A8), 18,901–18,907, doi:10.1029/1999JA000428.

Vakulin, I. I., O. S. Grafodatskii, V. I. Degtiarev, V. I. Dovgii, and G. A. Zherebtsov (1988), The radiation environment of the geostationary orbit for magnetically quiet conditions according to data from the Raduga communication satellites [in Russian], *Kosmicheskie Issledovaniia*, *26*, 120–126.

Volland, H. (1973), A semiempirical model of large-scale magnetospheric electric fields, *J. Geophys. Res.*, *78*(1), 171–180.

Wang, C.-P., M. Gkioulidou, L. R. Lyons, R. A. Wolf, V. Angelopoulos, T. Nagai, J. M. Weygand, and A. T. Y. Lui (2011), Spatial distributions of ions and electrons from the plasma sheet to the inner magnetosphere: Comparisons between THEMIS-Geotail statistical results and the Rice convection model, *J. Geophys. Res.*, *116*, A11216, doi:10.1029/2011JA016809.

Wang, C.-P., M. Gkioulidou, L. R. Lyons, and V. Angelopoulos (2012), Spatial distributions of the ion to electron temperature ratio in the magnetosheath and plasma sheet, *J. Geophys. Res.*, *117*, A08215, doi:10.1029/2012JA017658.

Whipple, E. C. (1981), Potentials of surfaces in space, *Rep. Prog. Phys.*, *44*, 1197–1250, doi:10.1088/0034-4885/44/11/002.

Wygant, J., D. Rowland, H. J. Singer, M. Temerin, F. Mozer, and M. K. Hudson (1998), Experimental evidence on the role of the large spatial scale electric field in creating the ring current, *J. Geophys. Res.*, *103*(A12), 29,527–29,544, doi:10.1029/98JA01436.

Zaharia, S., C. Z. Cheng, and J. R. Johnson (2000), Particle transport and energization associated with substorms, *J. Geophys. Res.*, *105*(A8), 18,741–18,752, doi:10.1029/1999JA000407.